

Disturbance amplification in boundary layers over thin wall films

Sandeep Saha, Jacob Page, and Tamer A. Zaki

Citation: *Physics of Fluids* **28**, 024108 (2016); doi: 10.1063/1.4940221

View online: <http://dx.doi.org/10.1063/1.4940221>

View Table of Contents: <http://scitation.aip.org/content/aip/journal/pof2/28/2?ver=pdfcov>

Published by the [AIP Publishing](#)

Articles you may be interested in

[On the relationship between the wall-shear-stress and transient-growth disturbances in a laminar boundary layer](#)

Phys. Fluids **22**, 054103 (2010); 10.1063/1.3415220

[Initial-value problem for three-dimensional disturbances in a compressible boundary layer](#)

Phys. Fluids **17**, 084106 (2005); 10.1063/1.2013261

[Weakly nonlinear analysis of boundary layer receptivity to free-stream disturbances](#)

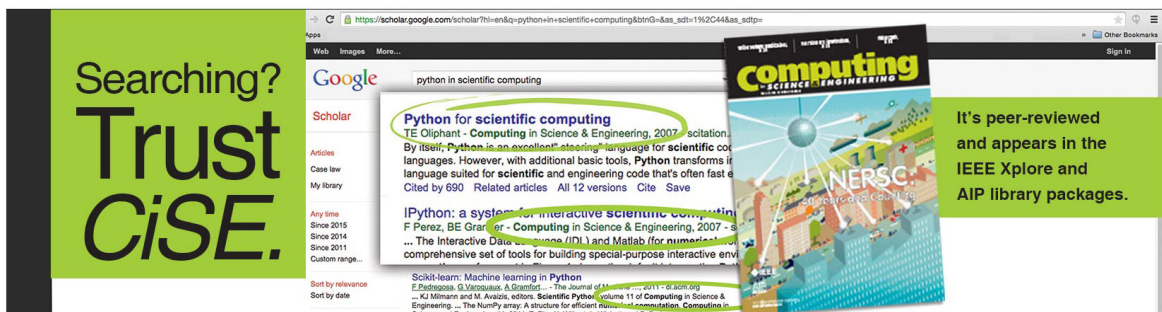
Phys. Fluids **14**, 1426 (2002); 10.1063/1.1456062

[Spatial theory of optimal disturbances in boundary layers](#)

Phys. Fluids **13**, 2097 (2001); 10.1063/1.1378070

[Optimal disturbances and bypass transition in boundary layers](#)

Phys. Fluids **11**, 134 (1999); 10.1063/1.869908



Searching? **Trust CiSE.**

Google Scholar search results for "python in scientific computing". The top result is "Python for scientific computing" by J. Orling, published in *Computing in Science & Engineering*, 2007. The snippet reads: "By itself, Python is an excellent teaching language for scientific computing languages. However, with additional basic tools, Python transforms into a language suited for scientific and engineering code that's often faster than C. Cited by 690. Related articles. All 12 versions. Cite. Save."

Other results include "IPython: a system for interactive scientific computing" by F. Perez, B.E. Granger, and "The Interactive Data Language (IDL) and Matlab for numerical computing" by a comprehensive set of tools for building special-purpose interactive environments.

Books shown: *Computing in Science & Engineering* (2007) and *NERSC: 20 Years and Counting*.

It's peer-reviewed and appears in the IEEE Xplore and AIP library packages.

Disturbance amplification in boundary layers over thin wall films

Sandeep Saha,^{1,2} Jacob Page,¹ and Tamer A. Zaki^{1,3,a)}

¹*Department of Mechanical Engineering, Imperial College, London SW7 2AZ, United Kingdom*

²*Department of Aerospace Engineering, Indian Institute of Technology, Kharagpur 721302, India*

³*Department of Mechanical Engineering, Johns Hopkins University, Baltimore, Maryland 21218, USA*

(Received 17 December 2014; accepted 16 December 2015; published online 16 February 2016)

In single-fluid boundary layers, streaks can amplify at sub-critical Reynolds numbers and initiate early transition to turbulence. Introducing a wall film of different viscosities can appreciably alter the stability of the base flow and, in particular, the transient growth of the perturbation streaks. The formalism of seminorms is used to identify optimal disturbances which maximize the kinetic energy in the two-fluid flow. An examination of optimal growth over a range of viscosity ratios of the film relative to the outer flow reveals three distinct regimes of amplification, each associated with a particular combination of the eigenfunctions. In order to elucidate the underlying amplification mechanisms, a model problem is formulated: An initial value problem is solved using an eigenfunction expansion and is used to compute the evolution of pairs of eigenfunctions. By appropriately selecting the pair, the initial value problem qualitatively reproduces the temporal evolution of the optimal disturbance, and provides an unambiguous explanation of the dynamics. Two regimes of transient growth are attributed to the evolution of the interface mode along with free-stream vortical modes; the third regime is due to the evolution of the interface and a discrete mode. The results demonstrate that a lower-viscosity film can effectively reduce the efficacy of the lift-up mechanism and, as a result, transient growth of disturbances. However, another mechanism of amplification of wall-normal vorticity arises due to the deformation of the two-fluid interface and becomes dominant below a critical viscosity ratio. © 2016 AIP Publishing LLC. [<http://dx.doi.org/10.1063/1.4940221>]

I. INTRODUCTION

Laminar-to-turbulence transition in boundary layers is sensitive to the flow configuration and environmental conditions. Even in a single-fluid zero-pressure-gradient boundary layer, various breakdown scenarios are possible.¹ One general distinction is between natural and bypass transition: The former takes place when the background disturbances are weak and proceeds via the amplification of discrete Tollmien–Schlichting waves and their secondary instability which ultimately leads to the inception of turbulent spots. Bypass transition, on the other hand, takes place when the free-stream turbulence level is appreciable. It is characterized by the formation of high-amplitude boundary-layer streaks and early breakdown to turbulence.² Recent direct numerical simulations³ have demonstrated that introducing a wall film with a carefully selected viscosity can stabilize the outer boundary layer and delay bypass transition. The streaks which precede transition onset were weaker in amplitude than in the single-fluid configuration, and the stabilizing influence of the film was evident despite the potential that the two-fluid interface introduces new instability mechanisms. The present study applies linear theory to examine the ability of a wall film with different viscosities

^{a)} Author to whom correspondence should be addressed. Electronic mail: t.zaki@jhu.edu

to weaken the pre-transitional boundary-layer streaks. This work therefore bridges two strands of research: instability of two-fluid flows and transient growth analysis in single-fluid boundary layers.

A. Two-fluid modal instabilities

In the context of two-fluid shear flows, research has primarily focused on discrete instability waves. In addition to the conventional Tollmien–Schlichting waves of the outer flow, three groups of discrete instability modes have been identified: the “soft” mode,⁴ “H” mode,⁵ and the high-Reynolds-number instability.⁶ The soft mode was established in the pioneering work by Yih.⁴ The long-wavelength instability arises from the viscosity mismatch across the two-fluid interface and can exist at any Reynolds number. However, this mode becomes stable when the lower layer is thinner and less viscous compared to the upper layer.^{7,8} Unlike the soft mode, the “H mode” discovered by Hooper and Boyd⁵ is unstable independent of the viscosity of the inner fluid. It is a short wavelength instability and is also due to the viscosity jump at the interface. There is no experimental evidence of this mode since a nominal level of surface tension is sufficient to stabilize this mechanism.⁹ The final instability exists at high Reynolds numbers, when the kinematic viscosity of the wall-bounded fluid is less than that of the upper fluid.⁶ The wavelength of the instability is on the order of the film thickness and is unaffected by surface tension. The instability derives energy largely from the Reynolds stress in the lower fluid and has its origin in a viscous layer near the wall.

Recent studies have examined the spatio-temporal character of these two-fluid instabilities and their evolution in the non-linear regime. For example, Valluri *et al.*¹⁰ demonstrated that channel flow with a thin wall-film is convectively unstable and that the amplifying soft mode leads to the formation of ligaments. On the other hand, the non-linear development of the instability waves for a thick wall film results in the formation of slug structures.¹¹ A combination of both two- and three-dimensional instabilities in channel flow can produce ligaments, sheets, or “interfacial turbulence” in different regions of the parameter space.¹² For spatially developing two-fluid flows, the non-linear parabolized stability equations have been formulated and applied to study intermodal energy transfer and the distortion to the mean flow.^{13,14}

In the present study, we focus on the stabilizing influence of a wall film on the outer boundary layer. Exponential instabilities can be avoided at moderate Reynolds numbers and when the wall film is less viscous with a nominal level of surface tension at the interface. As a result, linear disturbances can only exhibit transient amplification. Transient growth analyses are well established in the context of stability of single-fluid boundary layers and have received some attention in the context of subcritical two-fluid channel flows.^{15–18} They have also been applied to unstable configurations, such as core-annular pipe flow,¹⁹ two-fluid mixing layers,²⁰ and round viscous jets.²¹ The literature has not, however, addressed the two-fluid boundary-layer configuration which is analyzed herein.

B. Streaks in single-fluid boundary layers

Bypass transition in single-fluid boundary layers takes place in three major stages: The initial step is the receptivity of the boundary layer to free-stream disturbances. The second stage, which is the present focus, is the algebraic amplification of boundary-layer streaks. The final stage is the sporadic burst of turbulent spots caused by the secondary instabilities of the streaky base flow. The spots spread as they convect downstream and merge to form the fully turbulent boundary layer.

The extent to which a free-stream vortical disturbance perturbs a single-fluid boundary layer was examined by Jacobs and Durbin²² and later by Zaki and Saha.²³ Asymptotic analyses identified three important regimes based on the ratio $k_y^2 \nu / k_x \tau$, where k_y is the wall-normal wavenumber of the vortical mode, k_x is its streamwise wavenumber, ν is the viscosity, and τ is the mean shear.²³ When $k_y^2 \nu / k_x \tau \ll 1$, the boundary layer appears impermeable to free-stream disturbances – an effect known as “shear sheltering.”²⁴ In the reciprocal limit, $k_y^2 \nu / k_x \tau \gg 1$, shear-sheltering is ineffective and free-stream vortical modes permeate the boundary layer. An intermediate regime, $k_y^2 \nu / k_x \tau \sim O(1)$, is characterized by partial penetration of the vortical disturbances inside the shear.

In the context of a two-fluid boundary layer, it is intuitive to expect that a lower viscosity wall film would enhance shear-sheltering, since $k_y^2 \nu / k_x \tau$ decreases for lower ν and larger τ near the wall. However, Zaki and Saha²³ demonstrated that this trend is not monotonic: The viscosity of the wall film must decrease below a critical value in order for sheltering to be enhanced. It is therefore possible to reduce the boundary layer susceptibility to external forcing using a lower-viscosity film. Whether the penetrating disturbances will amplify to lower- or higher-levels than their single-fluid counterpart remains unknown.

Characteristics of boundary-layer streaks have been widely documented based on experiments^{25–28} and simulations.^{29–32} Their amplification at subcritical Reynolds numbers can be explained in terms of transient growth theory, i.e., the temporal or spatial evolution of optimal disturbances from initial conditions.^{33–35}

The solution of the linear perturbation equations as an initial value problem was proposed by Ellingsen and Palm.³⁶ They reported the existence of an inviscid, three-dimensional algebraic instability, which was previously overlooked due to Squire's transformation. Landahl³⁷ examined the temporal evolution of general localized perturbations. He predicted that the disturbance kinetic energy increases indefinitely with time due to the inviscid lift-up mechanism and that the streamwise extent of the disturbance grows with time which is consistent with rapid distortion theory.³⁸ The viscous initial value problem was subsequently solved in bounded flows.^{39,40} In boundary layers, Zaki and Durbin³¹ solved the initial value problem as a forced response problem where the wall-normal vorticity was driven by the wall-normal velocity perturbation. Resonance between the Orr–Sommerfeld forcing and the homogeneous Squire operator lead to a short time algebraic amplification of the response, followed by long-time viscous decay.

Butler and Farrell³³ computed the optimal initial condition which undergoes maximum transient amplification in wall-bounded flows. The energy growth is viewed as a result of the non-normality of the coupled system of the Orr–Sommerfeld and Squire equations.⁴¹ The same approach was adopted in the context of boundary layers. In both the temporal and spatial problems, the optimal disturbance was a streamwise oriented vortex, and the response is a streamwise elongated streak.^{34,35,42} The analysis also accurately predicts the spanwise spacing of the streaks to be on the order of the boundary layer thickness, consistent with observations from experiments and simulations.^{28,43}

In the present study, the influence of a wall-film of different viscosities on the transient amplification of disturbances in a boundary layer is investigated. The use of a wall-film as a strategy for bypass transition delay has recently been assessed by Jung and Zaki.³ Those authors used direct numerical simulations to demonstrate that boundary layer transition beneath free-stream turbulence can be shifted significantly downstream using a thin, less-viscous film. The linear analyses presented herein provide a foundation to explain their observations. A lower viscosity film absorbs the mean shear and can therefore reduce the transient growth of disturbances in the outer flow. However, the stronger near-wall shear, and the effectively higher Reynolds number due to the lower viscosity, can enhance transient amplification of disturbances near the wall. In addition, the viscosity mismatch at the interface can introduce new mechanisms of disturbance growth. Both the optimal disturbance analysis and the initial value problem are presented and, where new mechanisms of disturbance amplification arise, they are explained.

This paper is organized into six sections. In Sec. II, the procedure for finding optimal disturbances in the two-fluid boundary layer is introduced. Results from the optimal disturbance analysis are reported in Sec. III. In Sec. IV, an initial value problem describing the evolution of a monochromatic disturbance is solved and provides the basis for the discussion for the physical mechanisms of transient amplification in Sec. V. Finally, conclusions are drawn and key results are summarized in Sec. VI.

II. THEORETICAL FORMULATION

In this section, a framework is developed to compute optimal, temporal disturbances in two-fluid boundary layer flows.

A. Base flow

We consider a thin film of thickness $y = \delta_f(x)$ sheared by an outer boundary-layer flow. The two fluids are immiscible and support a viscosity discontinuity across the interface. In the subsequent stability analyses, a locally parallel flow is assumed. The base flow is computed from the large- x similarity solution for two-fluid boundary layers derived by Nelson, Alving, and Joseph.⁴⁴ In both fluids, the Blasius equation is satisfied,

$$\tilde{\nu}_\alpha \frac{d^3 F}{d\xi^3} + \frac{F}{2} \frac{d^2 F}{d\xi^2} = 0, \quad (1)$$

where $\alpha = 1$ in the top fluid and $\alpha = 2$ in the wall film. The similarity variable is $\xi = y\sqrt{U_\infty x/\nu_1}$, and the streamwise velocity is $U = U_\infty d_\xi F$. The similarity variable is based on properties of the outer fluid, so that $\tilde{\nu}_1 = 1$ and $\tilde{\nu}_2 = \nu_2/\nu_1$. The free-stream condition along with no slip at the rigid wall lead to the boundary conditions on F ,

$$d_\xi F(\infty) = 1, \quad F(0) = 0, \quad d_\xi F(0) = 0. \quad (2)$$

Furthermore, continuity of velocities and stresses is imposed across the interface,

$$[[F]] = 0, \quad [[d_\xi F]] = 0, \quad [[\tilde{\mu}_\alpha d_\xi^2 F]] = 0, \quad (3)$$

where $[[\bullet]] = (\bullet)_+ - (\bullet)_-$ is the jump in a quantity across the two-fluid interface. Throughout, variables are normalized by the top fluid reference quantities. For example, the Reynolds number is $R = U_\infty \delta_{sf}/\nu_1$, and the viscosity ratio is $m = \mu_2/\mu_1$.

Some example velocity profiles are reported in Figure 1. The wall-film thickness is $\delta_f = 0.1\delta_{sf}$, where δ_{sf} is the boundary layer 99% thickness for a single-fluid flow at the same Reynolds number. As the viscosity ratio is reduced, more of the shear is contained in the lower fluid. This is accompanied by a reduction in the boundary layer thickness.

B. Linear perturbation equations

Small perturbations are superimposed onto the parallel base flow, $\mathbf{U} = [U(y), 0, 0]$. After invoking a normal modes assumption in the streamwise and spanwise directions, $\psi'(\mathbf{x}, t) = \psi(y, t) \exp[i(k_x x + k_z z)]$, the disturbance evolution is described by the linearized Navier Stokes equations in each fluid,

$$ik_x u + \frac{\partial v}{\partial y} + ik_z w = 0, \quad (4a)$$

$$\rho \left(\frac{\partial u}{\partial t} + ik_x U u + v U' \right) = -ik_x p + \mu_\alpha \left(\frac{\partial^2 u}{\partial y^2} - k^2 u \right), \quad (4b)$$

$$\rho \left(\frac{\partial v}{\partial t} + ik_x U v \right) = -\frac{\partial p}{\partial y} + \mu_\alpha \left(\frac{\partial^2 v}{\partial y^2} - k^2 v \right), \quad (4c)$$

$$\rho \left(\frac{\partial w}{\partial t} + ik_x U w \right) = -ik_z p + \mu_\alpha \left(\frac{\partial^2 w}{\partial y^2} - k^2 w \right). \quad (4d)$$

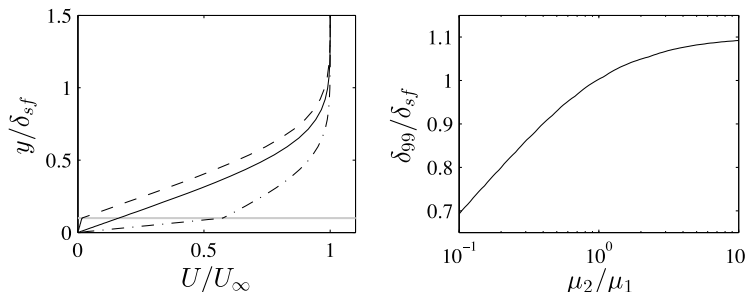


FIG. 1. (Left) Solutions to the two-fluid similarity equation, (---) $\mu_2 = 10\mu_1$, (—) $\mu_2 = \mu_1$, (— · —) $\mu_2 = 0.2\mu_1$. (Right) δ_{99} boundary layer thickness as a fraction of the thickness of a single fluid boundary layer. The film thickness $\delta_f = 0.1\delta_{sf}$.

The interface between the two fluids is a material surface, and small deformations are described by the linear kinematic condition,

$$\left(\frac{\partial f}{\partial t} + ik_x U f\right) \delta(y - \delta_f) = v \delta(y - \delta_f). \quad (5)$$

Integrated in y , Equation (5) yields the familiar interface evolution equation. The inclusion of the δ -function is necessary for the definition of certain inner products that appear in the optimization procedure. In the linear problem, matching conditions for the velocities and stresses are applied at the mean interface location, $y = \delta_f$,

$$[[u]] = -[[U']]f, \quad [[v]] = 0, \quad [[w]] = 0, \quad (6a)$$

$$[[\mu(\partial_y u + ik_x v)]] = -[[\mu U'']]f, \quad [[\mu(ik_z v + \partial_y w)]] = 0, \quad [[-p + 2\mu\partial_y v]] = \sigma k^2 f, \quad (6b)$$

where σ is the surface tension.

It is convenient to express the perturbation equations in operator form,

$$\frac{\partial}{\partial t} \mathcal{M} \phi - \mathcal{L} \phi \equiv \mathcal{A} \phi = 0, \quad (7)$$

where $\phi = [u, v, w, p, f]$ is the state vector and the operator \mathcal{A} contains the linearized Navier–Stokes equations. Assuming a time dependence $\phi(y, t) = \hat{\phi}(y) \exp(-i\omega t)$ leads to the eigenvalue problem,

$$-i\omega_j \mathcal{M} \hat{\phi}_j = \mathcal{L} \hat{\phi}_j. \quad (8)$$

C. Seminorm optimization

In optimal growth analyses, a measure of energy must be defined. Earlier studies of two-fluid flows have incorporated the interface displacement in this measure. For example, Yecko and Zaleski²⁰ included the potential energy of the interface when computing optimal disturbances in two-fluid mixing layers. However, in other flow configurations, the choice of norm is often constrained by convergence issues,^{45,46} and tuning factors were introduced to ensure convergence.^{15,16} This practice can obscure the physical interpretation of the term involving f . However, in the absence of such a term in the functional, there is no penalty associated with storing infinite “energy” in f at the initial time, which would lead to unbounded transient growth.

The physical problem at hand, namely, the delay of bypass transition using a wall film, has the perturbation kinetic energy as a natural choice for the objective functional. In order to optimize for this quantity while avoiding the issues mentioned above, the formalism of seminorms is adopted.^{35,47} A seminorm is a functional of the state vector with a non-trivial kernel. Therefore, in the present setup, the perturbation kinetic energy is one example of a seminorm since the interface deformation is absent. A complementary seminorm involving only f is used to constrain the initial interface deformation and allows us to search for initial disturbances which maximize the kinetic energy.

To formalize these ideas, the following global and local inner products are defined:

$$\langle \zeta, \vartheta \rangle = \int_0^T \int_0^\infty \bar{\zeta} \vartheta \, dy \, dt, \quad (9a)$$

$$(\zeta, \vartheta) = \int_0^\infty \bar{\zeta} \vartheta \, dy, \quad (9b)$$

where the bar indicates Hermitian transpose. The optimal disturbance, ϕ_o , maximizes the kinetic energy at some target time, T . The objective functional, a seminorm, can be defined using the local inner product,

$$\begin{aligned} J[\phi] &= \|\phi\|_u^2 = (\phi, \mathbf{E}\phi), \\ &= \int_0^\infty \bar{\phi} \mathbf{E} \phi \, dy, \end{aligned} \quad (10)$$

where $\mathbf{E} = \text{diag}(\rho, \rho, \rho, 0, 0)$. We define the complementary seminorm involving only f as $\|\phi_o\|_f^2 = (\phi_o, \mathbf{F}\phi_o) \equiv |f_o|^2$, where $\mathbf{F} = \text{diag}(0, 0, 0, 0, \delta(y - \delta_f))$. The interest in boundary layer streaks

focuses attention on purely vortical initial conditions, so the initial interface deformation is constrained to be zero, $\|\phi_o\|_f^2 = 0$. Additionally the optimal disturbance is normalized to unit initial kinetic energy, $\|\phi_o\|_u^2 = 1$.

Accounting for these constraints, the augmented Lagrangian for the optimization problem is

$$L[\phi, \phi^\dagger, \phi_o, \phi_o^\dagger, \{\lambda_j\}] = \underbrace{J[\phi(T)]}_{(i)} - \underbrace{\langle \phi^\dagger, \mathcal{A}\phi \rangle}_{(ii)} - \underbrace{(\phi_o^\dagger, \phi(t=0) - \phi_o)}_{(iii)} - \underbrace{\lambda_u(\|\phi_o\|_u^2 - 1)}_{(iv)} - \underbrace{\lambda_f\|\phi_o\|_f^2}_{(v)}. \quad (11)$$

The Lagrangian includes the objective functional (i) along with a system of constraints (ii)–(v). Constraint (ii) ensures the disturbance field satisfies the linear equations for all times, and so the associated Lagrange multiplier is the adjoint field, $\phi^\dagger(y, t)$. The third term on the right hand side, constraint (iii), ensures the initial disturbance is the optimal $\phi(t = 0) = \phi_o$. It is important to note that, in general, $\phi_o^\dagger \neq \phi^\dagger(t = 0)$. Terms (iv) and (v) are seminorm constraints on the initial velocity and interface deformation, respectively.

Optimal initial conditions that satisfy all constraints are obtained by setting the first variation of the Lagrangian equal to zero, $\delta L = 0$. This procedure is described in detail in [Appendix A](#). The result is a system of equations which are satisfied by the optimal disturbance. The original system of constraints is recovered,

$$\mathcal{A}\phi = 0, \quad \phi_o = \phi(t = 0), \quad \|\phi_o\|_u^2 = 1, \quad \|\phi_o\|_f^2 = 0. \quad (12)$$

Furthermore, the adjoint field is also required to satisfy its own evolution equations for all times,

$$\mathcal{A}^\dagger \phi^\dagger = 0. \quad (13)$$

The adjoint equations and boundary conditions are presented in [Appendix B](#). The system is closed with relationships between the forward and adjoint perturbation fields at the initial and target times,

$$\mathcal{M}\phi^\dagger(t = T) = 2\mathbf{E}\phi(t = T), \quad (14a)$$

$$2\lambda_u\mathbf{E}\phi(t = 0) + 2\lambda_f\mathbf{F}\phi(t = 0) = \mathcal{M}\phi^\dagger(t = 0). \quad (14b)$$

Equation (14b) provides the shape of the initial disturbance field and the magnitude is determined by the seminorm constraints.

The optimal disturbance satisfying this system of constraints is obtained using a simple iterative time-marching procedure, similar to that outlined by Luchini³⁵ and Schmid.⁴⁸

III. OPTIMAL GROWTH

Growth envelopes for a fixed pair of horizontal wavenumbers are reported in [Figure 2](#) for various viscosity ratios. The growth envelope, or energy gain, is defined by $G(t) = J[\phi(t)]$. The figure shows a significant reduction in transient growth over the viscous time scale, $t \sim O(R/k^2)$, when the film viscosity is reduced. Strikingly, there is also the emergence of a second peak in $G(t)$ at much longer times. Contrary to the short-time amplification, the second maximum is enhanced as the viscosity ratio is reduced. It will be shown subsequently that the two peaks are

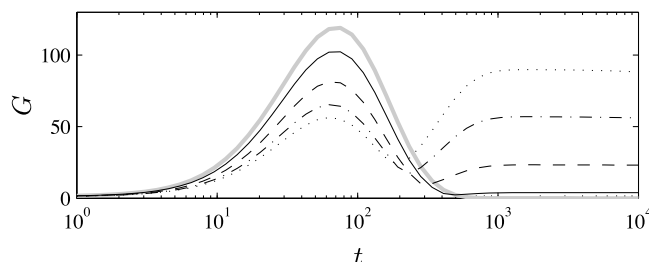


FIG. 2. Growth envelopes at $R = 800$ with $k_x = 0.001$, $k_z = 2$. The thick grey line is the single-fluid Blasius solution, (—) $m = 0.6$, (---) $m = 0.4$, (— —) $m = 0.3$, (·····) $m = 0.25$. The film thickness $\delta_f = 0.1\delta_{sf}$.

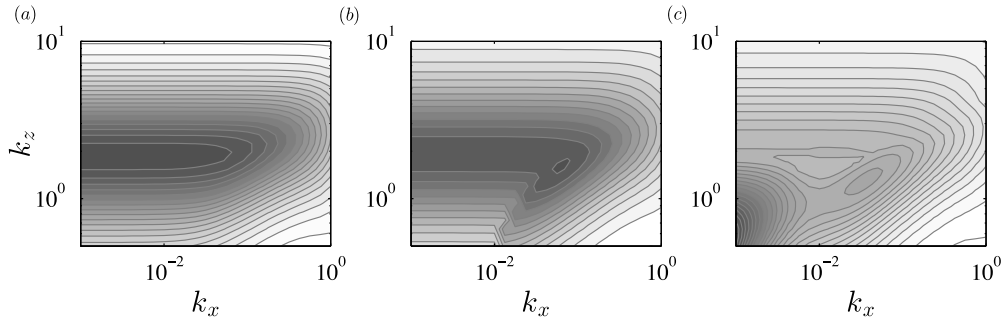


FIG. 3. (a) and (b) Contours of G_s at $R = 800$, $\delta_f = 0.1\delta_{sf}$: (a) $m = 0.6$; contours have a spacing of 5, the maximum contour level is 100. (b) $m = 0.35$; contours have a spacing of 5, the maximum contour level is 75. (c) Contours of G_{max} at $R = 800$, $\delta_f = 0.1\delta_{sf}$, with $m = 0.3$; contours have a spacing of 5, the maximum contour level is 145.

associated with different physical mechanisms. Note that surface tension is set to zero in Figure 2, $We^{-1} \equiv \sigma/\rho U_\infty^2 \delta_{sf} = 0$. The influence of finite surface tension is examined in Sec. III A.

Caution should be exercised in the interpretation of the long-time transient growth observed in Figure 2. Transition mechanisms in boundary layers exposed to free-stream disturbances often act on shorter time scales and, hence, these long-time scale perturbations might not play a significant role unless they have appreciable amplitudes ahead of the predicted peak. In addition, over such long times, the parallel flow assumption becomes increasingly inaccurate, particularly in the two-fluid configuration since the interface spreading rate differs from the boundary layer in the outer fluid.⁴⁴ Therefore we will initially focus our attention on short-time amplification, before presenting a qualitative discussion of the long-time growth.

The analysis is restricted to the short-time behaviour by stopping the optimization procedure after the first maximum in $G(t)$ is reached. This first maximum is denoted G_s , while the global maximum is termed G_{max} . In general the two peaks are well separated and this procedure is effective. Contours of G_s as a function of the horizontal wavenumber vector are reported for two viscosity ratios in Figures 3(a) and 3(b). For the more viscous of the two films, $m = 0.6$, the optimal structure is streamwise-independent, $k_x \rightarrow 0$. This is similar to the single-fluid configuration, although energy amplification is weakened with the wall-film as seen in Figure 2. This behaviour, namely, the weakening of the streamwise-independent optimal, is termed “regime 1.” The less viscous film, $m = 0.35$, exhibits a further damping of G_s across the entire wavenumber space. However, in this instance, the optimal disturbance shifts to a finite streamwise wavenumber. We term this finite- k_x optimal “regime 2.”

The influence of film thickness on the maximum short-time growth, $G_s^{opt} \equiv \max_{k_x, k_z} G_s$, in regimes 1 and 2 is examined in Figure 4. For a given $m < 1$, the reduction in transient growth is more pronounced with a thicker wall-film. Note that results for $m\delta_{sf}/\delta_f < 3$ have been omitted

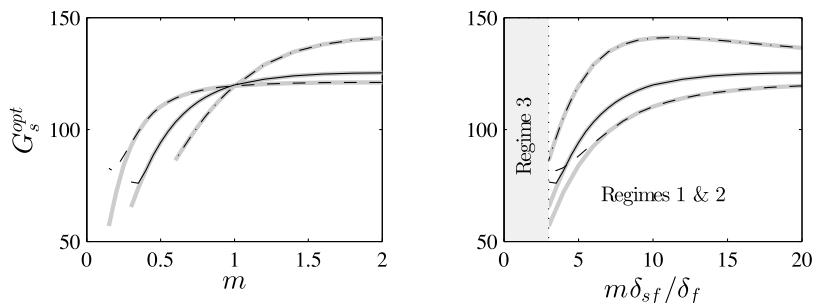


FIG. 4. Influence of film thickness on transient growth in regimes 1 and 2. The thick grey lines indicate the energy amplification in the optimal streamwise vortex, $k_x = 0$. Black lines correspond to the global optimal on the viscous time scale. Here (---) $\delta_f = 0.05\delta_{sf}$; (—) $\delta_f = 0.1\delta_{sf}$; (-·-) $\delta_f = 0.2\delta_{sf}$.

from Figure 4. Below this value, the growth envelopes no longer possess distinct maxima, and the long-time amplification cannot be distinguished from G_s . This long-time growth is denoted “regime 3.” Finally, note that the transition from the streamwise independent regime 1 to regime 2, which has a finite streamwise wavenumber, is only evident in the thinner films, $\delta_f \in [0.05, 0.1]\delta_{sf}$. The optimal for the thicker film, $\delta_f = 0.2\delta_{sf}$, remains at $k_x = 0$ over the range of film viscosities considered.

The majority of results will examine a single film thickness, $\delta_f = 0.1\delta_{sf}$. This particular choice is motivated by two main considerations: (i) Of the three film thicknesses in Figure 4, $\delta_f = 0.1\delta_{sf}$ exhibits the strongest reduction in the short-time amplification G_s^{opt} , approximately 35% relative to the single-fluid boundary layer. (ii) Both regimes 1 and 2 are evident in the short time optimal growth G_s^{opt} when $\delta_f = 0.1\delta_{sf}$.

With the limit on the final time removed, we can examine the long-time amplification (regime 3). This long-time growth is most pronounced at low viscosity ratios. Accordingly, contours of G_{max} are reported in Figure 3(c) for $m = 0.3$. In this figure, a small amount of surface tension, $We^{-1} = 10^{-6}$, has been included to stabilize the “H mode,” which becomes unstable for large horizontal wavenumbers. For the lower film viscosity considered in Figure 3(c), the most dangerous initial disturbance shifts back to very long streamwise lengthscales, $k_x \rightarrow 0$. This behaviour is similar to that found in regime 1 at short times. However, the G_{max} contours in Figure 3(c) indicate that the spanwise lengthscale is also increased. In fact, the global optimal has both $(k_x, k_z) \rightarrow 0$ and is not contained within the wavenumber range considered in Figure 3. This limit corresponds to a mean flow distortion. However, significant amplification is still obtained when $k_z = O(1)$, and attention will be focussed on this region of the parameter space.

A. The effect of surface tension

The influence of finite surface tension on optimal disturbances from each of the three regimes is examined in Figure 5. In all three cases, surface tension has a damping effect on both the short- and long-time transient growths. A similar stabilizing effect was reported for two-fluid modal instabilities.^{12,49}

Surface tension impacts the disturbance evolution through the normal stress jump across the interface (Equation (6b)), exerting a restoring stress proportional to the interface curvature, $-k^2$. Its effect on the short-time amplification reflects this dependence: Reduction in the first maximum, G_s , is most pronounced for the regime with the largest horizontal wavenumber, regime 1. However, a notable reduction in G_s is only observed for the largest surface tension considered in Figure 5. Therefore, we do not comment further on its effects in regimes 1 and 2.

The long-time amplification, most pronounced in regime 3, exhibits a much stronger dependence on surface tension despite the much lower horizontal wavenumber. The significant damping effect of surface tension at long-times merits further discussion and is explained in Sec. V in the context of the initial value problem solved in Sec. IV.

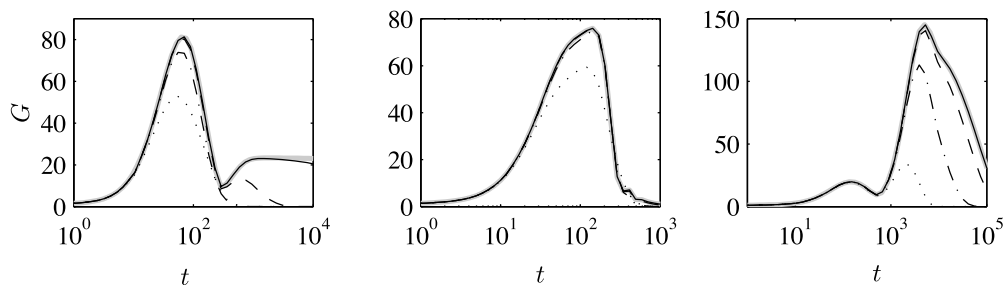


FIG. 5. Influence of surface tension on growth envelopes in the three regimes. From left to right: Regime 1, $m = 0.4$, $k_x = 0.001$, $k_z = 2$; regime 2, $m = 0.35$, $k_x = 0.056$, $k_z = 1.54$; regime 3, $m = 0.3$, $k_x = 0.001$, $k_z = 0.5$. Grey lines are the zero surface tension reference cases, $We^{-1} = 0$; (—) $We^{-1} = 10^{-6}$; (---) $We^{-1} = 10^{-4}$; (-·-) $We^{-1} = 10^{-3}$; (····) $We^{-1} = 10^{-2}$.

IV. A MODEL INITIAL VALUE PROBLEM

The optimal growth analyses have identified three regimes of transient growth in wavenumber space. While the results indicate the propensity for energy amplification, they do not explain the underlying mechanism. An understanding is sought by solving the initial value problem which governs the wall-normal vorticity response to decaying vertical velocity and interface modes. The solution to the initial value problem will be used in Sec. V to examine the relevant mechanisms which yield optimal growth.

A. Orr-Sommerfeld and Squire subsystems

We return to the linear perturbation equations in primitive variables (4a)-(4d), which can be reduced to the Orr-Sommerfeld and Squire equations for the normal velocity, v , and vorticity, $\eta \equiv ik_z u - ik_x w$, respectively. Orr-Sommerfeld and interface evolution equation (5) together form an autonomous subsystem,

$$\left(\frac{\partial}{\partial t} + ik_x U\right) \left(\frac{\partial^2}{\partial y^2} - k^2\right) v - ik_x U'' v - v_\alpha \left(\frac{\partial^2}{\partial y^2} - k^2\right)^2 v = 0, \quad (15a)$$

$$\left(\frac{\partial f}{\partial t} + ik_x U f\right) \delta(y - \delta_f) = v \delta(y - \delta_f). \quad (15b)$$

They are, however, two-way coupled due to the interface jump conditions,

$$[[v]] = 0, \quad [[\partial_y v]] = ik_x [[U']] f, \quad (16a)$$

$$[[\mu (\partial_y^2 + k^2) v]] = ik_x [[\mu U'']] f, \quad [[\rho [(\partial_t + ik_x U) \partial_y v - ik_x U' v] - \mu (\partial_y^2 - 3k^2) \partial_y v]] = \sigma k^4 f. \quad (16b)$$

Meanwhile the Squire equation and the associated jump conditions on the normal-vorticity are

$$\frac{\partial \eta}{\partial t} + ik_x U \eta - v_\alpha \left(\frac{\partial^2}{\partial y^2} - k^2\right) \eta = -ik_z U' v, \quad (17)$$

$$[[\eta]] = -ik_z [[U']] f, \quad [[\mu \partial_y \eta]] = -ik_z [[\mu U'']] f. \quad (18)$$

In Equations (15)–(18), there is one way coupling from the normal velocity and interface displacement to the normal vorticity: Squire equation (17) is forced by v , which tilts the mean spanwise vorticity, and also by f in jump conditions (18). The normal-velocity and interface equations can therefore be regarded as a homogeneous, autonomous subsystem. Assuming a solution ansatz $[v(y, t), f(t)] = [\hat{v}(y), \hat{f}] \exp(-i\omega^{\text{os}} t)$ results in an eigenvalue problem for the complex frequency, ω^{os} ,

$$-i\omega_j^{\text{os}} \begin{bmatrix} (d_y^2 - k^2) \hat{v}_j \\ \delta(y - \delta_f) \hat{f}_j \end{bmatrix} = \begin{bmatrix} ik_x U'' - (ik_x U - v_\alpha (d_y^2 - k^2))(d_y^2 - k^2) & 0 \\ \delta(y - \delta_f) & -ik_x U \delta(y - \delta_f) \end{bmatrix} \begin{bmatrix} \hat{v}_j \\ \hat{f}_j \end{bmatrix}. \quad (19)$$

The eigensolutions are denoted Orr-Sommerfeld modes. On the other hand, the Squire dynamics are regarded as a forced response problem in an approach similar to that adopted by Zaki and Durbin.³¹ The forcing is a known solution of Orr-Sommerfeld/interface system (19). The relevant eigenvalue problem is the homogeneous Squire equation,

$$-i\omega_j^{\text{sq}} \hat{\eta}_j^H = -ik_x U \hat{\eta}_j^H + v_\alpha (d_y^2 - k^2) \hat{\eta}_j^H. \quad (20)$$

The homogeneous Squire eigenfunctions do not have an associated vertical velocity or interface displacement and hence satisfy homogeneous jump conditions at the interface,

$$[[\hat{\eta}_j^H]] = 0, \quad [[\mu d_y \hat{\eta}_j^H]] = 0. \quad (21)$$

In general the two sets of eigenvalues, $\{\omega^{\text{os}}\}$ and $\{\omega^{\text{sq}}\}$, each consist of a finite number of discrete modes and a continuous branch. The continuous spectrum modes are oscillatory in the free stream and are characterized by a wall-normal wavenumber k_y . An example eigenvalue spectrum of the (v, f) subsystem is reported in Figure 6. There is an interface mode along with the continuous

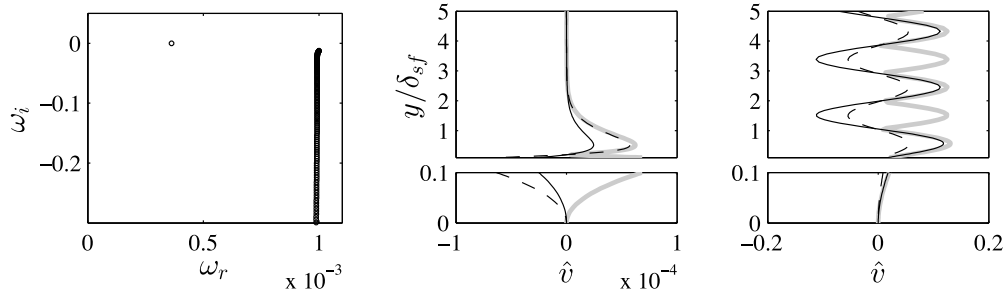


FIG. 6. Eigenvalue spectrum and example eigenfunctions of the (v, f) subsystem. (Left) Eigenvalue spectrum with $k_x = 0.001$, $k_z = \pi$, $R = 800$, $m = 0.3$, $\delta_f = 0.1\delta_{sf}$. (Centre) Interface mode, $\omega = 3.6 \times 10^{-4} - (3.5 \times 10^{-7})i$. (Right) Continuous mode, $\omega = 0.001 - 0.026i$. Grey line is the absolute value, (—) real, (---) imaginary component.

spectrum. Figure 6 also shows eigenfunctions of the interface mode and a continuous mode. The interface mode has a normal velocity component much smaller than the continuous mode. This observation is important in understanding the evolution of the normal velocity response in the two-fluid boundary layer.

The transient normal-vorticity response is now obtained by forcing the Squire equation with a single O-S mode. The forcing mode, $[v(y, t), f(t)] = [\hat{v}(y), \hat{f}] \exp(-i\omega_\zeta t)$, is labelled ω_ζ , where $\zeta = n$ corresponds to a mode from the discrete spectrum, whilst $\zeta = \tilde{k}_y$ is a continuous mode with wall-normal wavenumber \tilde{k}_y .

B. Solution to the Squire initial value problem

A solution to the forced Squire equation for a single fluid boundary layer was presented by Zaki and Durbin.³¹ They expressed the solution $\eta(y, t)$ to Equation (17) as an eigenfunction expansion in terms of homogeneous Squire modes (20). In their case, the modes satisfy all the boundary conditions and are straightforward to adopt. In the two-fluid problem, the homogeneous Squire modes are continuous across interface (21). However, in forced response problem (17), $\eta(y, t)$ must satisfy jump conditions (18). As a result, directly expanding $\eta(y, t)$ in terms of the homogeneous Squire eigenfunctions is not ideal.

Instead of η , we solve for a surrogate function, Ψ , which is continuous,

$$\Psi(y, t) = \eta(y, t) + ik_z U' f(t) g(y), \quad (22)$$

and satisfies the jump conditions implicitly. The function $g(y)$ must be continuous and differentiable over the interval $[0, \infty)$ in order for Ψ to be continuous and for η to satisfy the interfacial jump conditions. Moreover $g(y)$ should equal unity at the interface and zero at the wall. The choice of $g(y)$ does not affect the results and any $g(y)$ which satisfies the above criteria can serve the purpose of solving the initial value problem. In our particular case, we define $g(y) \equiv (y/\delta_f) \exp[(\delta_f - y)/\delta_{sf}]$. Thus the interfacial boundary conditions on Ψ are identical to those on homogeneous Squire modes (21) and Ψ can be conveniently expanded in terms of the homogeneous Squire eigenfunctions. Substitution into Squire equation (17) yields the evolution equation,

$$\frac{\partial \Psi}{\partial t} + ik_x U \Psi - \nu_\alpha \left(\frac{\partial^2}{\partial y^2} - k^2 \right) \Psi = \mathcal{F} e^{-i\omega_\zeta t}, \quad (23)$$

where the forcing term due to an O-S mode, $\hat{v}(y) \exp(-i\omega_\zeta t)$, is given by

$$\mathcal{F} = -ik_z \left[U' (\hat{v}(y) - \hat{v}(y_f) g(y)) + \nu_\alpha \left(\frac{\partial^2}{\partial y^2} - k^2 \right) (U' g(y)) \hat{f} \right].$$

Following Zaki and Durbin,³¹ we expand Ψ in terms of the homogeneous Squire eigenfunctions,

$$\Psi(y, t) = \sum_{n=1}^N b_n(t) \hat{\eta}_n^H(y) + \int_{k_y} b_{k_y}(t) \hat{\eta}_{k_y}^H(y) dk_y. \quad (24)$$

The expansion is substituted into Equation (23) and the amplitude coefficients, $b_n(t)$ and $b_{k_y}(t)$, are derived using the biorthogonality of $\hat{\eta}_j^H(y)$ and their adjoints $\hat{\eta}_j^{H\dagger}(y)$ (see Appendix B). Finally, one obtains

$$b_n(t) = b_n(0)e^{-i\omega_n t} - (\hat{\eta}_n^{H\dagger}, \rho \mathcal{F}) \left(\frac{e^{-i\omega_\zeta t} - e^{-i\omega_n t}}{i\omega_\zeta - i\omega_n} \right), \tag{25a}$$

$$b_{k_y}(t) = b_{k_y}(0)e^{-i\omega_{k_y} t} - (\hat{\eta}_{k_y}^{H\dagger}, \rho \mathcal{F}) \left(\frac{e^{-i\omega_\zeta t} - e^{-i\omega_{k_y} t}}{i\omega_\zeta - i\omega_{k_y}} \right), \quad k_y \neq \tilde{k}_y, \omega_{k_y} \neq \omega_\zeta, \tag{25b}$$

$$b_{k_y}(t) = b_{k_y}(0)e^{-i\omega_{k_y} t} - (\hat{\eta}_{k_y}^{H\dagger}, \rho \mathcal{F}) t e^{-i\omega_\zeta t}, \quad k_y = \tilde{k}_y, \omega_{k_y} = \omega_\zeta, \tag{25c}$$

where $b_n(t)$ are the amplitudes of the discrete modes and $b_{k_y}(t)$ are the amplitudes of the continuous modes. Note that the solution differentiates two cases: When the continuous Squire mode matches the forcing, resonance must be taken into account (25c). This behavior emerges because the eigen-spectra of the Orr-Sommerfeld and Squire operators have overlapping continuous branches. Finally, the normal vorticity η is obtained from Ψ using Equation (22).

V. MECHANICS OF ENERGY AMPLIFICATION

In this section, the solution of the initial value problem is invoked to explain the three regimes of energy amplification identified in the optimal growth analysis in Sec. III. We find that all three behaviours can be reproduced by forcing the Squire equation with an appropriate pair of Orr-Sommerfeld modes. The approach therefore provides a physical interpretation of each of the three regimes.

A. Regime 1: Damping of streamwise streaks

The first mechanism of transient growth identified in the optimization was the amplification of streamwise-independent structures. It was observed that a less-viscous wall film weakens the kinetic energy growth relative to the single fluid problem. An example growth envelope for this regime, along with the optimal disturbance field and its response is shown in Figure 7. The duration of the time integration has been extended to include the second peak in the growth envelope. The optimal disturbance is a row of counter-rotating streamwise vortices, while the response is a row of high- and low-speed streaks in the streamwise velocity. This behavior is familiar from the single-fluid problem:³³ the location of streamwise velocity maxima and minima coincide with regions of downwelling and upwelling by the vortices, which is consistent with the dominance of the lift-up mechanism. In addition, the interface location at the time of maximum amplification has been overlaid on the optimal disturbance field. It is significantly deformed from its initially flat configuration.

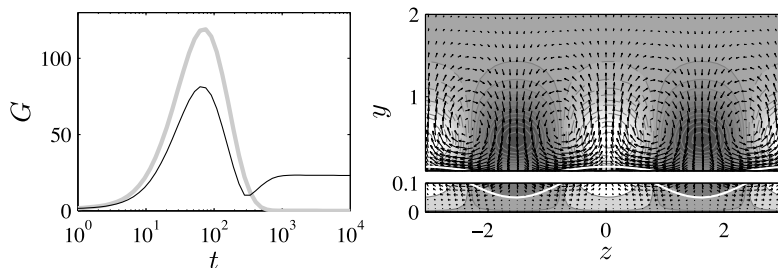


FIG. 7. (Left) Optimal growth envelopes for single fluid boundary layer (grey) and for a two-fluid boundary layer in regime 1 (black): $R = 800$, $\delta_f = 0.1\delta_{sf}$, $m = 0.4$, $k_x = 0.001$, $k_z = 2$. (Right) the optimal disturbance field, (v_o, w_o) , and response, $u(T)$ (contours) and $f(T)$ (white line), at the time of maximum amplification. The interface displacement has been normalized such that the maximum value is 0.05. Contours of $u(T)$ are from -10 to 10 , with a spacing of 1 in the outer fluid, 5 in the wall film.

We now outline a procedure to use the solution of the initial value problem to examine the trend in regime 1. The same methodology will be subsequently applied to the other regimes. First, the optimal disturbance leading to maximum amplification, $\phi_o(y)$, is written as a truncated expansion in the basis eigenfunctions (see Equation (8)),

$$\phi_o(y) \approx \sum_{j=1}^N D_j \hat{\phi}_j(y), \tag{26}$$

where $D_j = (\hat{\phi}_j^+, \mathcal{M} \phi_o)$ due to the biorthogonality relationship with the adjoint eigenfunctions (Appendix B). Since the optimal initial disturbance is primarily streamwise independent, it is nearly devoid of wall-normal vorticity, η . Therefore, we focus on the projection of the initial condition on the Orr-Sommerfeld spectrum. This projection will guide the selection of modes for the solution of the initial value problem.

In Figure 8, the amplitudes of the Orr-Sommerfeld modes are reported for an optimal initial disturbance in regime 1. The main contribution is due to continuous modes with decay rates $\omega_i \sim -10^{-2}$. Therefore, we seek to mimic the optimal disturbance evolution by forcing the Squire operator with an Orr-Sommerfeld eigenfunction representative of these high amplitude modes. The continuous modes have the dispersion relation,

$$\omega = k_x U_\infty - i\nu_1 (k_x^2 + k_y^2 + k_z^2). \tag{27}$$

The decay rate is set by the viscosity of the outer fluid, so the response can be meaningfully compared across a range of viscosity ratios, m , with a fixed wall-normal wavenumber, k_y . The most energetic mode $\omega_i = -10^{-2}$ has $k_y = 2$ for $k_x = 0.001$, $k_z = 2$.

Note that the Orr-Sommerfeld mode has an associated interface deformation and a particular normal vorticity. This is undesirable since setting the initial normal vorticity to zero violates the interfacial matching conditions. Furthermore, the optimal disturbance has $f(t = 0) = 0$. In order to nullify the interface deformation at $t = 0$ the interface mode is added to the initial condition, so that the initial disturbance takes the form

$$\begin{bmatrix} v(y, t) \\ f(t) \end{bmatrix} = A_{\bar{k}_y} \begin{bmatrix} \hat{v}_{\bar{k}_y} \\ \hat{f}_{\bar{k}_y} \end{bmatrix} e^{-i\omega_{\bar{k}_y} t} + A_{\text{int}} \begin{bmatrix} \hat{v}_{\text{int}} \\ \hat{f}_{\text{int}} \end{bmatrix} e^{-i\omega_{\text{int}} t}, \tag{28}$$

where $A_{\bar{k}_y} \hat{f}_{\bar{k}_y} + A_{\text{int}} \hat{f}_{\text{int}} = 0$. The initial vortical disturbance (not shown) is largely unaffected by the addition of the interface mode, since $|A_{\text{int}} \hat{v}_{\text{int}}| \ll |A_{\bar{k}_y} \hat{v}_{\bar{k}_y}|$, as was remarked with respect to Figure 6. Due to the lack of initial interface displacement, initial condition (28) satisfies the jump conditions at the interface.

The response due to this initial disturbance is reported in Figure 9 for a range of viscosity ratios, m . Since the response is contained with the shear, the calculation of the kinetic energy is

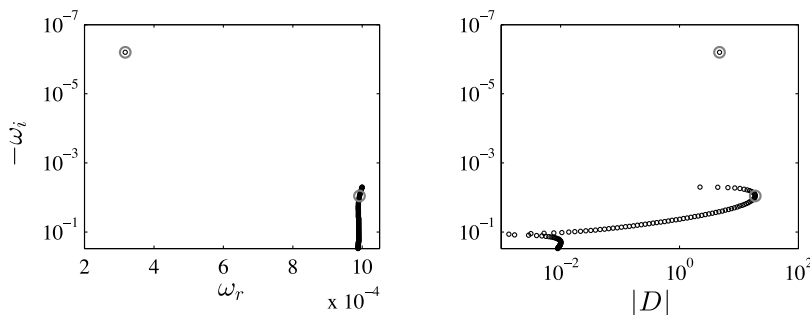


FIG. 8. (Left) Orr-Sommerfeld eigenvalue spectrum corresponding to the parameters in Figure 7, $m = 0.4$. (Right) Amplitude coefficients for the optimal disturbance. The two modes selected for the model initial value problem are highlighted by the larger dark grey circles.

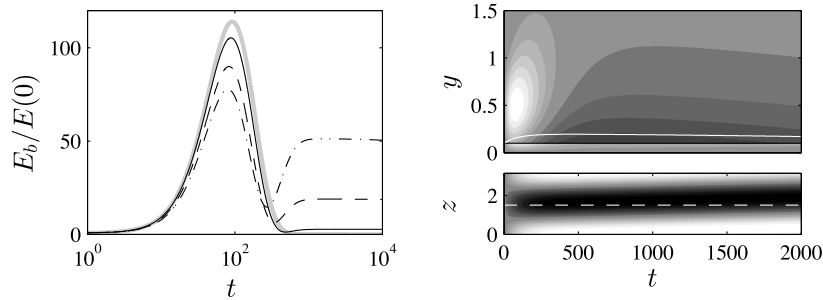


FIG. 9. Solution of the model problem in regime 1. (Left) Kinetic energy inside the boundary layer, grey line is the single fluid solution, “—” $m = 0.6$, “- - -” $m = 0.4$, “- · - · -” $m = 0.3$, “·····” $m = 0.25$. (Right) Evolution of the streamwise velocity field and interface displacement at a particular z location for $m = 0.4$. Top panel shows contours of $\Re[u(y, t)\exp(ik_z z)]$, i.e., at $x = 0$. The contour spacing is 2; the white line is the interface displacement, which has been given a maximum amplitude $|f|_{\max} = 0.1$. The spanwise location is indicated by the dashed line in the bottom panel, which shows contours of $\Re[f(t)\exp(ik_x x + ik_z z)]$.

limited to the boundary layer thickness,

$$E_b(t) = \frac{\rho L}{\delta_{99}} \int_0^{\delta_{99}} (|u|^2 + |v|^2 + |w|^2) dy, \quad (29)$$

where L is the height of the computational domain and is normalized by the initial disturbance energy (Equation (10)). The kinetic energy evolution shown in Figure 9 qualitatively agrees with the growth envelopes in Figure 2. Namely, the model problem captures the two peaks, their dependence on m and the time of maximum amplification.

In the right panel of Figure 9, the disturbance evolution is shown explicitly for one viscosity ratio, $m = 0.4$. The spanwise location was chosen to coincide with the centre of a negative streak. The initial vertical velocity disturbance inside the boundary layer causes an interface distortion and leads to the formation of streaks through the lift-up mechanism. Once the streaks have decayed above the film, the interface remains displaced, but the slower decay of u in the lower fluid means that a velocity disturbance of opposite sign is generated at $y > \delta_f$ and remains at long time.

This behavior can be explained through examination of the two eigenfunctions that form the initial condition. The amplitudes of the two modes were chosen such that the interface displacement is zero at $t = 0$. However, this cancellation is no longer maintained at later times since the continuous Orr-Sommerfeld mode decays much faster than the interfacial mode. Indeed, the streak in Figure 9 can be attributed to the continuous mode, while the existence of an appreciable $|u|$ at long times is due to the interface mode, which has an associated jump in normal vorticity (18). Our interest here is on the weakened streaks, and we will return to the long-time effects in more detail in the discussion of regime 3.

In the model initial value problem, the damped streaks grow on an inertial time scale and are described by the flow response to the decaying continuous mode. A small viscosity in the wall-film absorbs the majority of the base-flow shear close to the wall, while weakening the velocity gradient in the outer fluid. As a result, the effectiveness of the lift-up mechanism is enhanced in the film and weakened in the outer boundary layer. This competition between the two fluids is captured in Figure 10 where the lift-up term in the streamwise momentum equation has been integrated in the wall-normal direction. An examination of the relative contributions of the outer fluid and the wall-film for $\delta_f = 0.1\delta_{sf}$ reveals that lift-up is suppressed in the former but enhanced in the latter, as expected. In this instance, the weak v near the wall means that the contribution of the outer fluid is more effective, and lift-up is monotonically decreasing as the film viscosity is reduced. For thicker films, the further weakening of the mean shear in the outer fluid for a given m results in a further reduction in lift-up when $m < 1$, in agreement with the trend in G_s^{\max} seen in Figure 4. However, this trend is not maintained as $m \rightarrow 0$, reflecting the increasing contribution of the strong shear in the wall-film.

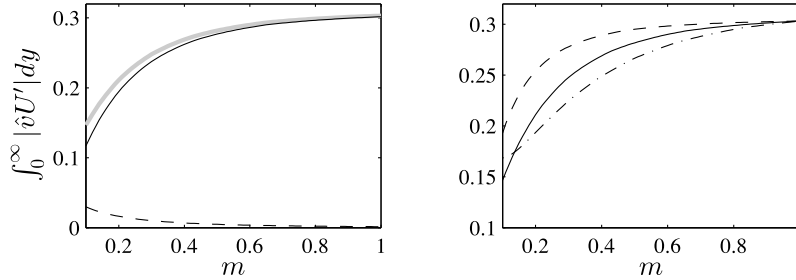


FIG. 10. Lift-up term, $\int_0^\infty |\hat{v}U'|dy$, as a function of the viscosity ratio m . (Left) Film thickness $\delta_f = 0.1\delta_{sf}$. Grey lines identifies $\int_0^\infty |\hat{v}U'|dy$, while the black lines are the same integral evaluated in the film (---) and in the top fluid (—). (Right) The integral $\int_0^\infty |\hat{v}U'|dy$ as a function of film thickness; (---) $\delta_f = 0.05\delta_{sf}$; (—) $\delta_f = 0.1\delta_{sf}$; (-·-·) $\delta_f = 0.2\delta_{sf}$. The eigenfunction, \hat{v} , belongs to the continuous spectrum, $k_x = 0.001$, $k_y = 2$, $k_z = 2$.

B. Regime 2: Transient growth due to discrete modes

In regime 2, the optimal disturbance shifts to non-zero k_x (see Sec. III). An example growth envelope for this regime is reported in Figure 11. Unlike regime 1, there is no amplification at long times. An example optimal disturbance and response at the time of maximum amplification are also shown in the figure. The disturbance is distinct from the streamwise oriented vortex discussed in connection with regime 1. However, the regions of high streamwise velocity fluctuations coincide with locations where the initial normal velocity perturbation is large. This indicates that amplification remains primarily due to the lift-up mechanism. The interface is also significantly deformed at the time of maximum amplification, similar to regime 1.

The optimal disturbance is again projected onto the linear stability eigenmodes. An example Orr-Sommerfeld eigenvalue spectrum is shown in Figure 12 alongside the corresponding amplitude coefficients. Along with the interface mode, the eigenfunctions include a stable Tollmien–Schlichting wave. This discrete mode has an amplitude an order of magnitude larger than any other eigenfunction.

Motivated by this observation, we mimic the optimal disturbance evolution by constructing an initial condition using one discrete O-S mode and the interface mode. The amplitude of the latter is chosen such that $f(t = 0) = 0$. Examples of the bimodal evolution in this regime for various values of the viscosity ratio, m , are provided in Figure 13. The solution to the model problem qualitatively captures the optimal growth behaviour, in particular the time of maximum amplification, but underpredicts the amplitude. An example disturbance evolution is provided in the right panel of Figure 13. Streaks grow and decay several times due to the finite frequency of the discrete mode which determines the phase speed in x and z for the resulting streaks. Again, the discontinuity in the streaks at the interface forces an interface deformation which is also shown in Figure 13.

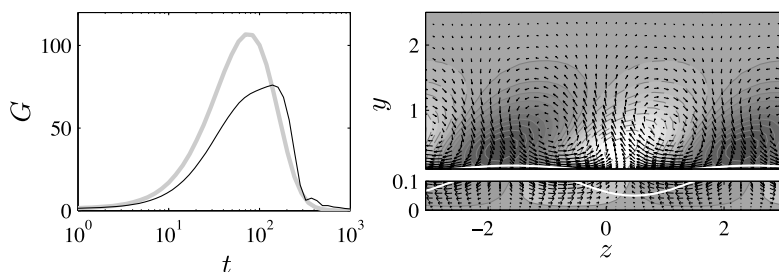


FIG. 11. (Left) Growth envelope for a two-fluid boundary layer in regime 2: $R = 800$, $\delta_f = 0.1\delta_{sf}$, $m = 0.35$, $k_x = 0.056$, $k_z = 1.54$; the grey line is the single-fluid solution. (Right) the optimal disturbance field, (v_o, w_o) , and response, $u(T)$ (contours) and $f(T)$ (white line), at the time of maximum amplification. The interface displacement has been normalized such that the maximum value is 0.05. Contours of $u(T)$ are from -10 to 10 , with a spacing of 1 in the outer fluid, 5 in the wall film.

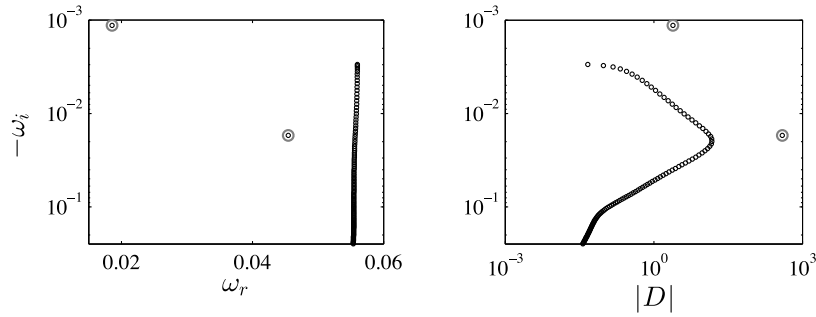


FIG. 12. (Left) Orr-Sommerfeld eigenvalue spectrum corresponding to the parameters in Figure 11, $m = 0.35$. (Right) Amplitude coefficients for the optimal disturbance. The two modes selected for the model initial value problem are highlighted by the larger dark grey circles.

C. Regime 3: Long-time amplification due to the interface mode

Finally we consider the long-time amplification, or regime 3. An example growth envelope for this regime is reported in Figure 14 alongside the optimal disturbance field. The curve $G(t)$ shows a similar trend to that seen in regime 1, although the second peak is much stronger. This indicates the dominance of the contribution by the interface. The mechanism was alluded to briefly in the discussion of regime 1 and is considered here in more detail. The occurrence of the second peak at very long times suggests that it is less relevant to transitional flows where the earlier growth mechanisms are likely to dominate. However, the sharp rise in the energy curve towards the second peak starts much earlier and can therefore be of interest.

The optimal disturbance and response shown in Figure 14 are unfamiliar—The spanwise and wall-normal lengthscales are much larger than those associated with the streamwise vortex of regime 1. Furthermore, the maxima/minima in the streamwise velocity do not coincide with regions of high $|v_o|$, which suggests that lift-up does not play a key role at such long times. Rather, the wall-normal location of $|u|_{\max}$ is on the interface itself.

The amplitudes of the basis Orr-Sommerfeld modes in the optimal disturbance are reported in Figure 15. The eigenvalue spectrum contains only an interface mode and the continuous spectrum, similar to regime 1. However, the continuous spectrum modes with the largest amplitude have a decay rate an order of magnitude smaller than in regime 1, $\omega_i \sim -10^{-3}$. This indicates the dominance of large scales, since $\omega_i \propto k_y^2$, and is consistent with observations of Figure 14.

The interface mode and a continuous mode with decay rate $\omega_i = -0.002$ are used to construct the initial disturbance for the model problem. The continuous mode produces a streak, while the interface mode is responsible for the amplification at long times. Example energy evolutions are shown in

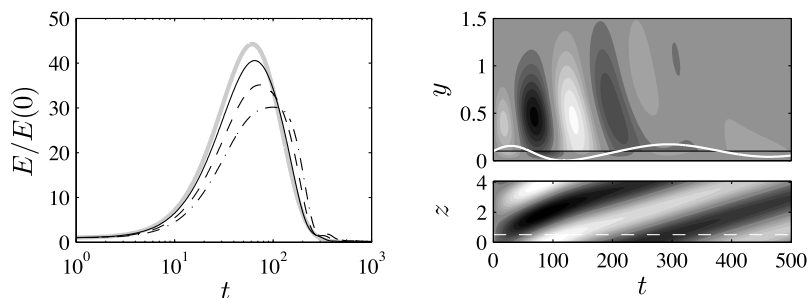


FIG. 13. Solution of the model problem for regime 2, $R = 800$, $\delta_f = 0.1\delta_{sf}$, $k_x = 0.056$, $k_z = 1.54$. (Left) Kinetic energy evolution, grey line is the single fluid solution, “—” $m = 0.6$, “- - -” $m = 0.4$, “- · - ·” $m = 0.35$. (Right) Evolution of the streamwise velocity field and interface displacement at a particular z location for $m = 0.35$. Top panel shows contours of $\Re[u(y, t)\exp(ik_z z)]$, i.e., at $x = 0$. The contour spacing is 1; the white line is the interface displacement, which has been given a maximum amplitude $|f|_{\max} = 0.1$. The spanwise location is indicated by the dashed line in the bottom panel, which shows contours of $\Re[f(t)\exp(ik_x x + ik_z z)]$.

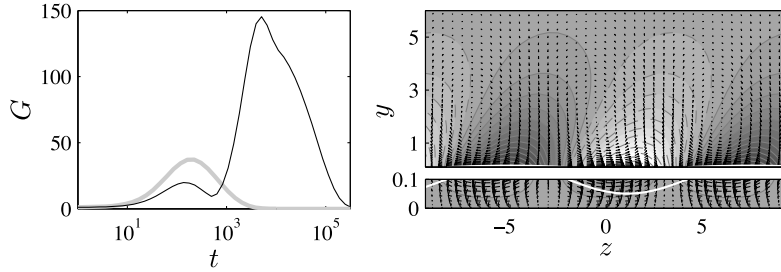


FIG. 14. (Left) Growth envelope for a two-fluid boundary layer in regime 3: $R = 800$, $\delta_f = 0.1\delta_{sf}$, $m = 0.3$, $k_x = 0.001$, $k_z = 0.5$. (Right) the optimal disturbance field, (v_o, w_o) , and response, $u(T)$ (contours) and $f(T)$ (white line), at the time of maximum amplification. The interface displacement has been normalized such that the maximum value is 0.05. Contours of $u(T)$ are from -13 to 13 with a spacing of 1 .

the left panel of Figure 16. Good agreement between the solution of the model problem (Figure 16) and the growth envelope (Figure 14) is observed. The energy growth at long time is enhanced as the viscosity ratio is reduced, while the strength of the first peak decreases.

A disturbance evolution for $m = 0.3$ is displayed in the right panel of Figure 16. Just as in regime 1, there is an initial streak generated by the decaying continuous mode. The long-time growth resulting from the perturbed interface is significantly more pronounced. The low frequency of the interface mode (for $m = 0.3$, $\omega_r \approx 0.0004$) and the associated phase speed are captured in the figure which spans a very long time period.

The enhanced amplification at lower film viscosities due to the interface deformation mechanism can be explained by the jump in u across the interface, $\llbracket u \rrbracket = -\llbracket U' \rrbracket f$. Rewriting the difference in U' in terms of m , we obtain

$$\llbracket u \rrbracket = \left(\frac{1 - m}{m} \right) U'_1(\delta_f) f. \tag{30}$$

This equation is proportional to $1/m$ for small m . Reducing the viscosity of the film enhances the jump in the mean shear, which means that a larger u fluctuation is required for a given f . In Figure 17, the energy associated with the interface mode for a fixed $\hat{f} = 1$ and a fixed horizontal wavenumber is plotted as a function of m . The energy behaves as $[(1 - m)U'_+/m]^2$; it is determined by the jump in streamwise velocity (30). This trend is established because the velocity field associated with the interface mode is due purely to an interface displacement. The interface mode is also slowly decaying compared to the viscous decay rate across the range of viscosities considered.

The optimal growth analyses in Sec. III demonstrated that the significant growth in regime 3 can be suppressed by finite surface tension, and we now briefly examine this effect in the context of the initial value problem. The long-time amplification has been attributed above to a slowly decaying interface mode. The initial amplitude of this mode was selected such that there was no initial interface

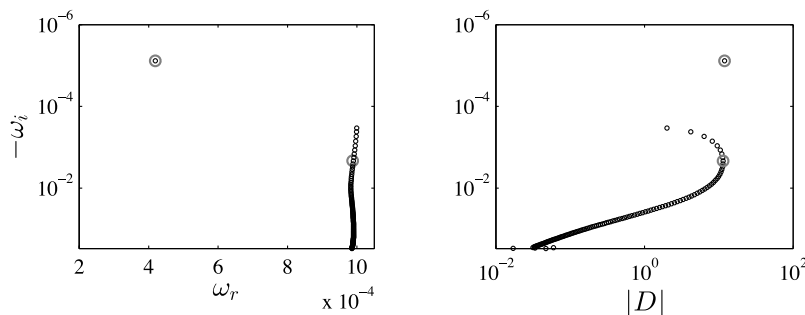


FIG. 15. (Left) Orr-Sommerfeld eigenvalue spectrum corresponding to the parameters in Figure 14, $m = 0.3$. (Right) Amplitude coefficients for the optimal disturbance. The two modes selected for the model initial value problem are highlighted by the larger dark grey circles.

deformation, and thus surface tension influences the long-time evolution in three ways: (i) Modifying the interface deformation associated with the *continuous mode*, which controls the interface amplitude once the inertial streaks have decayed (see Equation (28)); (ii) altering the kinetic energy of the interface mode for a given \hat{f} ; and (iii) changing the decay rate of the interface mode.

The three effects described above are examined in Figure 18 for a particular viscosity ratio, $m = 0.3$, and with varying surface tension. The interface displacement associated with the continuous mode and the kinetic energy density of the interface mode increase with stronger surface tension. Both effects thus favour an increase in the growth envelope. The weakened long-time growth can therefore be attributed solely to the decay rate of the interface mode, which becomes more rapid as the level of surface tension is increased.

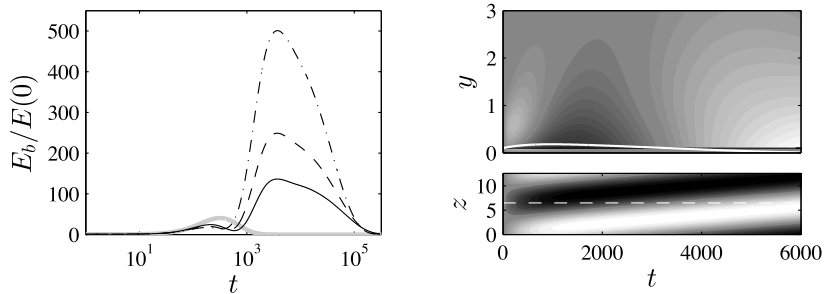


FIG. 16. Solution of the model problem for regime 3, $R = 800$, $\delta_f = 0.1\delta_{sf}$, $k_x = 0.001$, $k_z = 0.5$. (Left) Kinetic energy evolution, grey line is the single fluid solution, “—” $m = 0.3$, “- - -” $m = 0.25$, “- · -” $m = 0.2$. (Right) Evolution of the streamwise velocity field and interface displacement at a particular z location for $m = 0.3$. Top panel shows contours of $\Re[u(y, t)\exp(ik_z z)]$, i.e., at $x = 0$. The contour spacing is 1; the white line is the interface displacement, which has been given a maximum amplitude $|f|_{\max} = 0.1$. The spanwise location is indicated by the dashed line in the bottom panel, which shows contours of $\Re[f(t)\exp(ik_x x + ik_z z)]$.

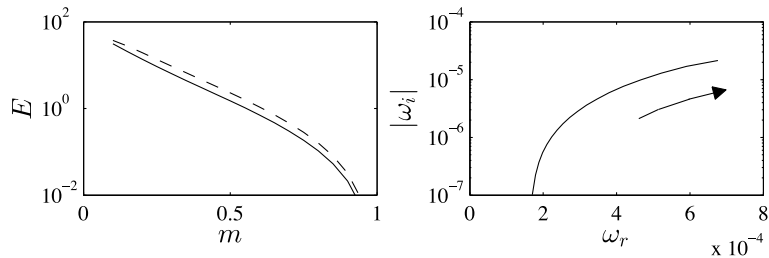


FIG. 17. (Left) Energy of the interface mode for a fixed $|\hat{f}| = 1$ as a function of the viscosity ratio, m , with $k_x = 0.001$, $k_z = 0.5$, $R = 800$, $\delta_f = 0.1\delta_{sf}$. Dashed line is the quantity $[(1 - m)U'_+/m]^2$. (Right) Complex frequency of the interface mode with varying m , the direction of decreasing m is indicated by the arrow.

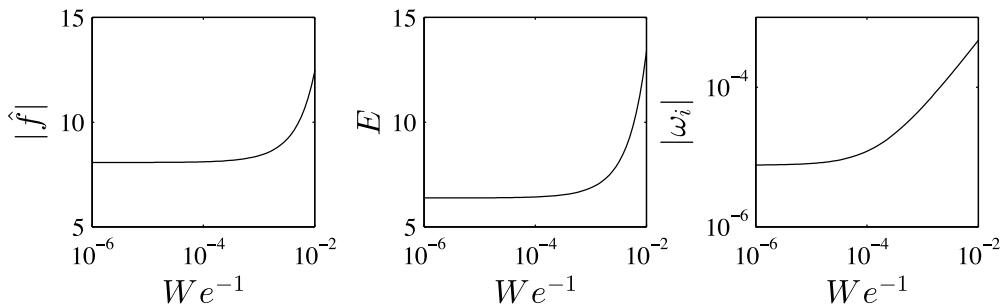


FIG. 18. Impact of surface tension in the model initial value problem. From left to right: Interface displacement of the continuous mode; kinetic energy in the interface mode for a unit displacement, $|\hat{f}| = 1$; decay rate of the interface mode. Here $R = 800$, $k_x = 0.001$, $k_z = 0.5$, $m = 0.3$.

VI. CONCLUSION

The temporal amplification of linear perturbations in a boundary layer above a less-viscous wall-film was examined. An optimization procedure using seminorms was employed to find the most dangerous initial conditions. Results of these transient growth calculations revealed three regimes of optimal disturbance. In order to explain the mechanics behind each of the regimes, an initial value problem for the normal-vorticity response to a decaying vertical velocity mode was solved. The solution provided insight into the three regimes: each of the behaviors could be replicated by forcing the normal vorticity equation with just two modes.

Regime 1 was the classical streamwise-independent vortex and was initially dominant as $m < 1$. Energy growth was damped by the wall-film. The energy amplification was captured in the initial value problem by forcing the normal vorticity equation with a continuous and the interface modes. It was observed that the effectiveness of lift-up was weakened by the redistribution of the mean shear into the film. The interface mode resulted in a second, weaker peak in the energy at longer times. Regime 2, which is also associated with amplification on the inertial time scale, appeared when $m \leq 0.35$ for $\delta_f = 0.1\delta_{s,f}$ and had finite streamwise wavenumber. Disturbance amplification in this regime was due to the influence of a stable Tollmien–Schlichting wave.

Extension of the optimization time to much longer horizons led to the identification of regime 3. Like regime 1, the optimal in this instance retained streamwise independence. Physically, the long-time growth derives from the fact that the jump in streamwise velocity perturbation caused by the interface displacement becomes stronger as the film viscosity is reduced. As a result, a larger u is established for a given f . The kinetic energy amplification is damped by surface tension, and the very long time scale of this regime suggests that it will most commonly be preceded by faster instability mechanisms. However, it highlights the possibility for the interface displacement mechanism to contribute to disturbance growth since the amplification process commences long before the optimal time.

The results presented provide an explanation of the mechanism by which a wall film can delay transition in boundary layers beneath free-stream turbulence and complement recent non-linear simulations.³ A judicious choice of the film viscosity can significantly weaken the amplification of boundary layer streaks, while avoiding any interfacial instabilities. Weaker streak distortions reduce the likelihood of secondary instability^{50,51} and hence delay transition to turbulence. The present study focussed on linear, temporal amplification in parallel flow. Future studies should consider the influence of a spatially developing mean flow, as well as the influence of additional effects, such as density stratification.

APPENDIX A: DETAILS OF THE OPTIMIZATION PROBLEM

The augmented Lagrangian for the optimization problem defined in the text is (cf. Equation (11)),

$$L[\phi, \phi^\dagger, \phi_o, \phi_o^\dagger, \{\lambda_j\}] = J[\phi(T)] - \langle \phi^\dagger, \mathcal{A}\phi \rangle - (\phi_o^\dagger, \phi(t=0) - \phi_o) - \lambda_u(\|\phi_o\|_u^2 - 1) - \lambda_f\|\phi_o\|_f^2. \quad (\text{A1})$$

Initial disturbances devoid of an interface displacement which maximize the kinetic energy at the target time T are found by setting the first variation to zero,

$$\delta L = \underbrace{\left\langle \frac{\delta L}{\delta \phi}, \delta \phi \right\rangle}_{(a)} + \underbrace{\left\langle \frac{\delta L}{\delta \phi^\dagger}, \delta \phi^\dagger \right\rangle}_{(b)} + \underbrace{\left\langle \frac{\delta L}{\delta \phi_o}, \delta \phi_o \right\rangle}_{(c)} + \underbrace{\left\langle \frac{\delta L}{\delta \phi_o^\dagger}, \delta \phi_o^\dagger \right\rangle}_{(d)} + \underbrace{\sum_j \frac{\delta L}{\delta \lambda_j} \delta \lambda_j}_{(e)} = 0. \quad (\text{A2})$$

Each term must independently vanish. Term (a) is considered first,

$$\frac{\delta L}{\delta \phi} = 2\mathbf{E}\phi(T) - \frac{\delta}{\delta \phi} \langle \phi^\dagger, \mathcal{A}\phi \rangle - \phi_o^\dagger = 0. \quad (\text{A3})$$

To compute the remaining gradient in the expression above, the definition of the adjoint is used,

$$\langle \phi^\dagger, \mathcal{A}\phi \rangle = \langle \mathcal{A}^\dagger \phi^\dagger, \phi \rangle + \mathcal{B}, \quad (\text{A4})$$

where \mathcal{B} denotes boundary terms. In [Appendix B](#), the term \mathcal{B} is found explicitly, and after the appropriate choice of boundary conditions,

$$\mathcal{B} = (\phi^\dagger, \mathcal{M}\phi)|_T - (\phi^\dagger, \mathcal{M}\phi)|_0, \quad (\text{A5})$$

where the subscripts T and 0 signify target and initial times, respectively. Using this expression, term (a) becomes

$$\frac{\delta L}{\delta \phi} = -\mathcal{A}^\dagger \phi^\dagger + 2\mathbf{E}\phi(T) - \mathcal{M}\phi^\dagger(T) + \mathcal{M}\phi^\dagger(0) - \phi_o^\dagger = 0 \quad (\text{A6})$$

and is rendered zero through three equalities. First, the adjoint equations hold for all times,

$$\mathcal{A}^\dagger \phi^\dagger = 0. \quad (\text{A7})$$

The second equality determines final conditions for the adjoint problem in terms of the forward variables,

$$\mathcal{M}\phi^\dagger(T) = 2\mathbf{E}\phi(T). \quad (\text{A8})$$

Finally, we obtain the identity,

$$\phi_o^\dagger = \mathcal{M}\phi^\dagger(0), \quad (\text{A9})$$

which will be revisited subsequently. Gradient term (b) recovers the constraint that the linear equations in the forward problem are satisfied,

$$\frac{\delta L}{\delta \phi^\dagger} = -\mathcal{A}\phi = 0. \quad (\text{A10})$$

In (c), we obtain initial conditions for the forward problem in terms of the adjoint variables,

$$\frac{\delta L}{\delta \phi_o} = \phi_o^\dagger - 2\lambda_u \mathbf{E}\phi_o - 2\lambda_f \mathbf{F}\phi_o = 0. \quad (\text{A11})$$

Recalling [\(A9\)](#), the above expression becomes

$$2\lambda_u \mathbf{E}\phi(0) + 2\lambda_f \mathbf{F}\phi(0) = \mathcal{M}\phi^\dagger(0). \quad (\text{A12})$$

Term (d) recovers the constraint,

$$\frac{\delta L}{\delta \phi_o^\dagger} = \phi_o - \phi(0) = 0, \quad (\text{A13})$$

whilst (e) yields the seminorm constraints,

$$\frac{\delta L}{\delta \lambda_u} = 1 - \|\phi_o\|_u^2 = 0, \quad \frac{\delta L}{\delta \lambda_f} = -\|\phi_o\|_f^2 = 0. \quad (\text{A14})$$

This result sets the relative magnitude of the components of the state vector at $t = 0$. The wall-normal shape of the initial disturbance is found from Equation [\(A12\)](#). An iterative method, described in [Sec. II](#), is used to ensure all of the constraints are satisfied.

APPENDIX B: ADJOINT EQUATIONS

In this appendix, the adjoint equations and their boundary conditions are presented. Using the inner product introduced in Equation [\(9\)](#), the adjoint operator is defined according to

$$\langle \phi^\dagger, \mathcal{A}\phi \rangle = \langle \mathcal{A}^\dagger \phi^\dagger, \phi \rangle + \mathcal{B}. \quad (\text{B1})$$

This expression was used in [Appendix A](#) in the formulation of the optimization problem. Here, however, we present the full form of \mathcal{B} and derive a set of matching conditions for the adjoint variables at the interface to arrive at the expression quoted in [\(A5\)](#).

Forming the inner product on the left hand side of (B1) and integrating by parts, the following set of equations for the adjoint “velocity” and “pressure” are obtained,

$$ik_x u^\dagger + \frac{\partial v^\dagger}{\partial y} + ik_z w^\dagger = 0, \quad (\text{B2})$$

$$-\rho \left(\frac{\partial u^\dagger}{\partial t} + ik_x U u^\dagger \right) = ik_x p^\dagger + \mu \left(\frac{\partial^2 u^\dagger}{\partial y^2} - k^2 u^\dagger \right), \quad (\text{B3a})$$

$$-\rho \left(\frac{\partial v^\dagger}{\partial t} + ik_x U v^\dagger - U' u^\dagger \right) = \frac{\partial p^\dagger}{\partial y} + \mu \left(\frac{\partial^2 v^\dagger}{\partial y^2} - k^2 v^\dagger \right), \quad (\text{B3b})$$

$$-\rho \left(\frac{\partial w^\dagger}{\partial t} + ik_x U w^\dagger \right) = ik_z p^\dagger + \mu \left(\frac{\partial^2 w^\dagger}{\partial y^2} - k^2 w^\dagger \right). \quad (\text{B3c})$$

Note that manipulation of the above system can produce adjoint “Orr-Sommerfeld” and “Squire” equations. The adjoint vertical vorticity is $\eta^\dagger \equiv ik_x w^\dagger - ik_z u^\dagger$.

Integrating the time derivatives in the original system of equations produces one contribution to the boundary term \mathcal{B} ,

$$\int_0^\infty \left[\bar{u}^\dagger \rho u + \bar{v}^\dagger \rho v + \bar{w}^\dagger \rho w + \bar{f}^\dagger \delta(y - \delta_f) f \right]_0^T dy \equiv (\phi^\dagger, \mathcal{M} \phi)|_T - (\phi^\dagger, \mathcal{M} \phi)|_0. \quad (\text{B4})$$

The terms in (B4) were used to relate the forward and adjoint variables at the initial and final times in Appendix A.

The remaining contributions to \mathcal{B} can be eliminated with the correct choice of boundary conditions on the adjoint variables. Homogeneous conditions are applied on the adjoint velocity, \mathbf{u}^\dagger , at the wall, $y = 0$, and in the free-stream, $y \rightarrow \infty$. The adjoint variables also satisfy a set of jump conditions at the two-fluid interface,

$$\llbracket u^\dagger \rrbracket = 0, \quad \llbracket v^\dagger \rrbracket = 0, \quad \llbracket w^\dagger \rrbracket = 0, \quad (\text{B5a})$$

$$\llbracket \mu (\partial_y u^\dagger + ik_x v^\dagger) \rrbracket = 0, \quad \llbracket \mu (ik_z v^\dagger + \partial_y w^\dagger) \rrbracket = 0, \quad \llbracket -p^\dagger - 2\mu \partial_y v^\dagger \rrbracket = f^\dagger. \quad (\text{B5b})$$

In addition, additional sources are introduced in the adjoint interface evolution equation,

$$\begin{aligned} \left(-\frac{\partial f^\dagger}{\partial t} - ik_x U f^\dagger \right) \delta(y - \delta_f) &= \left(\llbracket \mu U'' \rrbracket - \mu_- \llbracket U' \rrbracket \frac{\partial}{\partial y} \right) u_-^\dagger \delta(y - \delta_f) \\ &\quad - \left(\sigma k^2 + ik_x \mu_- \llbracket U' \rrbracket \right) v_-^\dagger \delta(y - \delta_f), \end{aligned} \quad (\text{B6})$$

where the subscript “-” indicates quantities evaluated at the interface approached from below.

Similar to the forward equations, the adjoint operator can be decomposed,

$$\mathcal{A}^\dagger \phi^\dagger \equiv -\frac{\partial}{\partial t} \mathcal{M} \phi^\dagger - \mathcal{L}^\dagger \phi^\dagger = 0. \quad (\text{B7})$$

The corresponding eigenvalue problem is

$$i\omega_j^\dagger \mathcal{M} \hat{\phi}_j^\dagger = \mathcal{L}^\dagger \hat{\phi}_j^\dagger. \quad (\text{B8})$$

The adjoint eigenfunctions and those of the forward problem are biorthogonal,

$$(\hat{\phi}_m^\dagger, \mathcal{M} \hat{\phi}_n) = \delta_{mn}, \quad (\text{B9})$$

where the eigenfunctions have been assumed to be appropriately normalized.

¹ M. V. Morkovin, E. Reshotko, and T. Herbert, “Transition in open flow systems—A reassessment,” *Bull. Am. Phys. Soc.* **39**, 1882 (1994).

² T. A. Zaki, “From streaks to spots and on to turbulence: Exploring the dynamics of boundary layer transition,” *Flow, Turbul. Combust.* **91**, 451–473 (2013).

³ S. Y. Jung and T. A. Zaki, “The effect of a low-viscosity near-wall film on bypass transition in boundary layers,” *J. Fluid Mech.* **747**, 330–360 (2015).

⁴ C. S. Yih, “Instability due to viscosity stratification,” *J. Fluid Mech.* **27**, 337–352 (1967).

- ⁵ A. P. Hooper and W. G. C. Boyd, "Shear-flow instability at the interface between viscous fluids," *J. Fluid Mech.* **128**, 507–528 (1983).
- ⁶ A. P. Hooper and W. G. C. Boyd, "Shear-flow instability due to a wall and a viscosity discontinuity at the interface," *J. Fluid Mech.* **179**, 201–225 (1987).
- ⁷ Y. Renardy, "The thin-layer effect and interfacial stability in a two-layer Couette flow with similar liquids," *Phys. Fluids* **30**, 1627–1637 (1987).
- ⁸ F. Charru and E. J. Hinch, "'Phase diagram' of interfacial instabilities in a two-layer Couette flow and mechanism of the long-wave instability," *J. Fluid Mech.* **414**, 195–223 (2000).
- ⁹ E. J. Hinch, "A note on the mechanism of the instability at the interface between two shearing fluids," *J. Fluid Mech.* **144**, 463–465 (1984).
- ¹⁰ P. Valluri, L. Ó. Naraigh, H. Ding, and P. D. M. Spelt, "Linear and nonlinear spatio-temporal instability in laminar two-layer flows," *J. Fluid Mech.* **656**, 458–480 (2010).
- ¹¹ P. Valluri, P. D. M. Spelt, C. J. Lawrence, and G. Hewitt, "Numerical simulation of the onset of slug initiation in laminar horizontal channel flow," *Int. J. Multiphase Flow* **34**, 206–225 (2007).
- ¹² L. Ó. Naraigh, P. Valluri, D. Scott, I. Bethune, and P. D. M. Spelt, "Linear instability, nonlinear instability and ligament dynamics in three-dimensional laminar two-layer liquid-liquid flows," *J. Fluid Mech.* **750**, 464–506 (2014).
- ¹³ L. C. Cheung and T. A. Zaki, "Linear and nonlinear instability waves in spatially developing two-phase mixing layers," *Phys. Fluids* **22**, 052103 (2010).
- ¹⁴ L. C. Cheung and T. A. Zaki, "A nonlinear PSE method for two-fluid shear flows with complex interfacial topology," *J. Comput. Phys.* **230**, 6756–6777 (2011).
- ¹⁵ M. J. South and A. P. Hooper, "Linear growth in two-fluid plane Poiseuille flow," *J. Fluid Mech.* **381**, 121–139 (1999).
- ¹⁶ S. V. Malik and A. P. Hooper, "Linear stability and energy growth of viscosity stratified flows," *Phys. Fluids* **17**, 024101 (2005).
- ¹⁷ S. V. Malik and A. P. Hooper, "Three-dimensional disturbances in channel flows," *Phys. Fluids* **19**, 052102 (2007).
- ¹⁸ P. Yecko, "Disturbance growth in two-fluid channel flow: The role of capillarity," *Int. J. Multiphase Flow* **34**, 272–282 (2008).
- ¹⁹ A. Orazzo, G. Coppola, and L. de Luca, "Disturbance growth in core-annular flow," *J. Fluid Mech.* **747**, 44–72 (2014).
- ²⁰ P. Yecko and S. Zaleski, "Transient growth in two-phase mixing layers," *J. Fluid Mech.* **528**, 43–52 (2005).
- ²¹ S. A. Boronin, J. J. Healey, and S. S. Sazhin, "Non-modal stability of round viscous jets," *J. Fluid Mech.* **716**, 96–119 (2013).
- ²² R. G. Jacobs and P. A. Durbin, "Shear sheltering and the continuous spectrum of the Orr-Sommerfeld equation," *Phys. Fluids* **10**(8), 2006–2011 (1998).
- ²³ T. A. Zaki and S. Saha, "On shear sheltering and the structure of vortical modes in single and two-fluid boundary layers," *J. Fluid Mech.* **626**, 113–148 (2009).
- ²⁴ J. C. R. Hunt and P. A. Durbin, "Perturbed vortical layers and shear sheltering," *Fluid Dyn. Res.* **24**, 375–404 (1999).
- ²⁵ P. S. Klebanoff, "Effect of freestream turbulence on the laminar boundary layer," *Bull. Am. Phys. Soc.* **10**, 1323 (1971).
- ²⁶ J. M. Kendall, "Studies on laminar boundary-layer receptivity to freestream turbulence near a leading edge," in *Boundary Layer Stability and Transition to Turbulence*, edited by D. C. Reda, H. L. Reed, and R. Kobayashi, ASME FED. 114, 23 (1991).
- ²⁷ K. J. A. Westin, A. V. Boiko, B. G. B. Klingmann, V. V. Kozlov, and P. H. Alfredsson, "Studies on laminar boundary layer receptivity to free-stream turbulence near a leading edge," *J. Fluid Mech.* **281**, 193–218 (1994).
- ²⁸ M. Matsubara and P. H. Alfredsson, "Disturbance growth in boundary layers subjected to free-stream turbulence," *J. Fluid Mech.* **430**, 149–168 (2001).
- ²⁹ R. G. Jacobs and P. A. Durbin, "Simulations of bypass transition," *J. Fluid Mech.* **428**, 185–212 (2001).
- ³⁰ L. Brandt, P. Schlatter, and D. Henningson, "Transition in boundary layers subject to free-stream turbulence," *J. Fluid Mech.* **517**, 167–198 (2004).
- ³¹ T. A. Zaki and P. A. Durbin, "Mode interaction and the bypass route to transition," *J. Fluid Mech.* **531**, 85–111 (2005).
- ³² K. P. Nolan and T. A. Zaki, "Conditional sampling of transitional boundary layers in pressure gradients," *J. Fluid Mech.* **728**, 306–339 (2013).
- ³³ K. M. Butler and B. F. Farrell, "Three dimensional optimal perturbation in viscous shear flow," *Phys. Fluids A* **4**, 1637–1650 (1992).
- ³⁴ P. Andersson, M. Berggren, and D. S. Henningson, "Optimal disturbances and bypass transition in boundary layers," *Phys. Fluids* **11**, 134–150 (1999).
- ³⁵ P. Luchini, "Reynolds-number-independent instability of the boundary layer over a flat surface: Optimal perturbations," *J. Fluid Mech.* **404**, 289–309 (2000).
- ³⁶ T. Ellingsen and E. Palm, "Stability of linear flow," *Phys. Fluids* **18**, 487–488 (1975).
- ³⁷ M. T. Landahl, "A note on an algebraic instability of inviscid parallel shear flows," *J. Fluid Mech.* **98**, 243–251 (1980).
- ³⁸ O. M. Phillips, "Shear-flow turbulence," *Annu. Rev. Fluid Mech.* **1**, 245–264 (1969).
- ³⁹ L. H. Gustavsson and L. S. Hultgren, "A resonance mechanism in plane Couette flow," *J. Fluid Mech.* **98**, 149–159 (1980).
- ⁴⁰ L. H. Gustavsson, "Resonant growth of three-dimensional disturbances in plane Poiseuille flow," *J. Fluid Mech.* **112**, 253–264 (1981).
- ⁴¹ P. J. Schmid and D. S. Henningson, *Stability and Transition in Shear Flows* (Springer-Verlag, 2001).
- ⁴² S. C. Reddy and D. S. Henningson, "Energy growth in viscous channel flows," *J. Fluid Mech.* **252**, 209–238 (1993).
- ⁴³ S. Nagarajan, S. K. Lele, and J. H. Ferziger, "Leading-edge effects in bypass transition," *J. Fluid Mech.* **572**, 471–504 (2007).
- ⁴⁴ J. J. Nelson, A. E. Alving, and D. D. Joseph, "Boundary layer flow of air over water on a flat plate," *J. Fluid Mech.* **284**, 159–169 (1995).
- ⁴⁵ T. L. van Noorden, P. A. M. Boomkamp, M. C. Knaap, and T. M. M. Verheggen, "Transient growth in parallel two-phase flow: Analogies and differences with single-phase flow," *Phys. Fluids* **10**, 2099 (1998).
- ⁴⁶ P. J. Olsson and D. S. Henningson, "Optimal disturbance growth in watertable flow," *Stud. Appl. Math.* **94**, 183–210 (1995).

- ⁴⁷ D. Foures, C. Caulfield, and P. Schmid, "Variational framework for flow optimization using seminorm constraints," *Phys. Rev. E* **86**, 026306 (2012).
- ⁴⁸ P. J. Schmid, "Nonmodal stability theory," *Annu. Rev. Fluid Mech.* **39**, 129–162 (2007).
- ⁴⁹ K. Isakova, J. O. Pralits, R. Repetto, and M. R. Romano, "A model for the linear stability of the interface between aqueous humor and vitreous substitutes after vitreoretinal surgery," *Phys. Fluids* **26**, 124101 (2014).
- ⁵⁰ N. J. Vaughan and T. A. Zaki, "Stability of zero-pressure-gradient boundary layer distorted by unsteady Klebanoff streaks," *J. Fluid Mech.* **681**, 116–153 (2011).
- ⁵¹ M. J. P. Hack and T. A. Zaki, "Streak instabilities in boundary layers beneath free-stream turbulence," *J. Fluid Mech.* **741**, 280–315 (2014).